



## Phases study for AgNb(Ta,W)O<sub>3</sub> lead-free antiferroelectric ceramics

Zhilun Lu<sup>a,\*</sup>, Yubo Zhu<sup>b</sup>, Dongyang Sun<sup>c</sup>, Bowen Wang<sup>d</sup>, Dawei Wang<sup>e</sup>, Sarah Day<sup>f</sup>, Ge Wang<sup>g,\*\*</sup>

<sup>a</sup> School of Chemical and Process Engineering, University of Leeds, Leeds, LS2 9JT, UK

<sup>b</sup> Department of Materials Science and Engineering, Sir Robert Hadfield Building, Mappin Street, Sheffield, S1 3JD, UK

<sup>c</sup> School of Computing, Engineering and the Built Environment, Edinburgh Napier University, Edinburgh, EH10 5DT, UK

<sup>d</sup> School of Engineering and Materials Science, Queen Mary University of London, London, E1 4NS, UK

<sup>e</sup> Functional Materials and Acousto-Optic Instruments Institute, School of Instrumentation Science and Engineering, Harbin Institute of Technology, Harbin, 150080, China

<sup>f</sup> Diamond Light Source Ltd, Harwell Science and Innovation Campus, Didcot, Oxfordshire, UK

<sup>g</sup> Department of Materials, University of Manchester, Manchester, S13 9PL, UK

### ABSTRACT

Uncovering lead-free materials with an exceptionally high recoverable energy density is vital for the creation of future pulse power capacitors. This study determined that introducing Tungsten (W) and Tantalum (Ta) into the Nb-site of AgNbO<sub>3</sub> lead-free antiferroelectric ceramics, while offsetting this with vacancies at the Ag-site, can effectively maintain the electrical homogeneity. Additionally, employing this co-doping approach can secure the antiferroelectric phases by lowering the necessary temperatures for M1-M2 and M2-M3 phase transitions. This may prove advantageous in the creation of novel AgNbO<sub>3</sub>-based energy storage ceramics. The use of *in-situ* high-resolution synchrotron powder x-ray diffraction (SPXD) at varying temperatures revealed for the first time that in 10 at% W doped AgNbO<sub>3</sub>, the M1 and M2 phases in the temperature range of -193 to ~150 °C are more appropriately fitted as the non-polar *Pbcm* space group, whereas the M3 phase aligns with the mixed of non-polar *Pbcm* and polar *Pmc*<sub>21</sub> space groups.

### 1. Introduction

The pivotal role of dielectric capacitors, with their high power density and swift charge-discharge rates, cannot be overstated in sophisticated pulse power systems. However, their potential applications are currently constrained by their suboptimal energy density when compared with batteries and electrochemical capacitors [1–5]. This underscores the urgent need for dielectric capacitors with augmented energy storage capabilities.

Lead-based antiferroelectrics have been the focus of extensive research in the past decade due to their superior energy storage capabilities. However, their inherent toxicity presents environmental and commercial challenges, necessitating the search for lead-free alternatives [6–8]. The main lead-free antiferroelectric materials that could potentially replace lead-based antiferroelectric ceramics are NaNbO<sub>3</sub> (NN) [9–13] and AgNbO<sub>3</sub> (AN) [14–16]. AN, when sintered in an oxygen atmosphere (oxygen partial pressure = 1), can easily become densified. Moreover, it possesses desirable characteristics such as stable antiferroelectric phase at room temperature and a high maximum polarization ( $P_{\max}$ ) post-phase transition (around 52 μC/cm<sup>2</sup> under an electric

field of 22 MV/m). These advantages make AN a promising and viable candidate material to replace lead-based antiferroelectric ceramics [17].

In the quest to enhance the energy density of AN-based ceramics, various doping strategies have been adopted. These include: i) The incorporation of a diverse range of dopants, such as Strontium (Sr), Calcium (Ca), Bismuth (Bi), Lanthanum (La), Samarium (Sm), Gadolinium (Gd), and others, into the Ag site represents one approach [18–23]. This tactic diversifies the ceramic's physical and chemical properties, contributing to a better-rounded performance profile. ii) As it stands, tantalum (Ta) is the only element employed for doping at the niobium (Nb) site. It is reported that the use of Ta as a dopant proves highly effective in augmenting  $E_b$ , which enhances the overall performance of the ceramics [16,24,25]. iii) Another popular strategy involves co-doping at the Ag and Nb sites. This technique often includes Sm/Nd/Ce and Ta co-doping and has been demonstrated in several studies [16,26]. iv) The introduction of a minuscule proportion of MnO<sub>2</sub> is another strategy utilized. This process results in the reduction of leakage current and grain size. Such modifications prove instrumental in amplifying the dielectric breakdown strength ( $E_b$ ), thereby improving the energy density [27,28]. Among the various types of doped AN-based

\* Corresponding author.

\*\* Corresponding author.

E-mail addresses: [z.lu@leeds.ac.uk](mailto:z.lu@leeds.ac.uk) (Z. Lu), [ge.wang@manchester.ac.uk](mailto:ge.wang@manchester.ac.uk) (G. Wang).

<https://doi.org/10.1016/j.rineng.2023.101447>

Received 25 June 2023; Received in revised form 9 August 2023; Accepted 21 September 2023

Available online 23 September 2023

2590-1230/© 2023 The Authors. Published by Elsevier B.V. This is an open access article under the CC BY license (<http://creativecommons.org/licenses/by/4.0/>).

ceramics, those doped with Gd, and Sm have achieved particularly high recoverable energy density of 4.5, and 5.2 J cm<sup>-3</sup>, respectively [20,29]. Meanwhile, ceramics doped/co-doped with Ta achieved values of 6.3, 6.5 and 7.37 J cm<sup>-3</sup> [16,24,30].

Recently, our research has identified that aliovalent doping in the Ag-site combined with Nb-site vacancies presents a pioneering approach for engineering AN-based ceramics that boast superior energy storage performance [31]. However, the effects of incorporating doping elements other than Ta into the Nb-site, especially when paired with Ag-site vacancies remain unexplored. Consequently, this study seeks to address this gap in knowledge. The current work investigates the replacement of Nb with tungsten (W) and/or Ta, which is accompanied by Ag-site vacancies, to achieve a balanced valence state. While this manuscript does not provide the energy density of AN-based ceramics, it offers a detailed study of the crystal structure, microstructure, and electrical and dielectric properties of the ceramics. Such comprehensive analyses serve as a solid foundation for understanding the phase transitions prompted by this innovative doping strategy, which is geared towards improving the energy storage properties of AN-based ceramics.

## 2. Experimental work

Ag<sub>1-x</sub>W<sub>x</sub>Nb<sub>1-x</sub>O<sub>3</sub>, Ag<sub>1-x</sub>W<sub>x</sub>Nb<sub>0.8-x</sub>Ta<sub>0.2</sub>O<sub>3</sub> ( $x = 0.05$  and  $0.10$ ), abbreviated as AW5, AW10, AW5T and AW10T, ceramics were fabricated by a solid-state reaction, involving Ag<sub>2</sub>O (>99%, Acros Organics), WO<sub>3</sub> (>99.9%, Sigma-Aldrich), Nb<sub>2</sub>O<sub>5</sub> (>99.9%, Sigma-Aldrich) and Ta<sub>2</sub>O<sub>5</sub> (>99.9%, Sigma-Aldrich) raw chemicals. The fabrication process started with the preparation of stoichiometric quantities of dried raw powders. These powders underwent a ball-milling process for 6 h with yttria-stabilized zirconia (YSZ) media in isopropanol. Subsequently, the wet powders were dried 16 h at 80 °C and then calcined for another 6 h at 900 °C under an oxygen atmosphere (5 °C/min heating and cooling). This was followed by another round of ball-milling for 6 h. The milling speed for all processes is set at 300 rpm. These treated powders were then uniaxially compressed into pellets with a diameter of 8 mm and thickness of ~0.5 mm. Finally, these pellets were sintered for 4 h at 1060–1100 °C under an oxygen atmosphere (5 °C/min heating and cooling).

X-ray diffraction (XRD) analyses were performed using a Bruker D2 phaser benchtop system with CuK $\alpha$  ( $\lambda = 1.5406$  Å) radiation. The surface morphology of the ceramics was investigated with the use of a Hitachi S4800 FE-SEM. The samples were prepared by subjecting them to a 120-s gold coating process utilizing an EMITECH K550X sputter coater from Quorumtech, UK. Subsequently, the gold-coated samples were observed using the FE-SEM set at a 10 kV acceleration voltage equipped with backscattered electron (BSE) and energy dispersive X-ray spectroscopy (EDS) detectors. The settings for these detectors were specifically calibrated at an acceleration voltage of 20 kV and a sample distance of 18 mm. Frequency and temperature-dependent permittivity and dielectric loss were measured from room temperature up to 500 °C, using an Agilent 4184 A precision LCR meter. This was done on pellets that had gold electrodes coated on their opposing parallel sides. Impedance spectroscopy (IS) data were collected over a frequency range of 20 Hz to 1 MHz using an Agilent E4980A analyzer. A geometric correction of the IS data was performed using ZView software.

High-resolution synchrotron powder x-ray diffraction (SPXD) was performed at Beamline I11, Diamond Light Source. Ceramic pellet specimens were crushed into fine powder and loaded into 0.2 mm capillary. The 1-D SPXD patterns were recorded using an energy of 15 keV (wavelength 0.825711 Å) and temperature was controlled between -193 °C and 227 °C by means of the Cryostream Plus. Full-pattern Rietveld refinements were carried out using Topas 6 software to extract crystallographic information.

## 3. Results and discussion

The XRD patterns of the AWx and AWxT ceramics are depicted in Fig. 1. All the diffraction peaks shown in the XRD can be accurately attributed to a singular orthorhombic perovskite structure, consistent with pure AN [16]. This demonstrates that the formation of solid solutions is effectively achieved using either Tungsten (W) with Ag-site vacancies or W/Tantalum (Ta) co-doping with Ag-site vacancies. For ease of comparison, the crystal planes associated with the peaks are marked in a cubic arrangement in Fig. 1. Upon magnifying the cubic {200}<sub>c</sub> peak, it is evident that the splitting associated with the orthorhombic structure ( $\{220\}_O + \{008\}_O$ ) is less pronounced when Ta doping is implemented, while the introduction of W doping leaves it unaffected. In comparison with AW5T and AW10T (Fig. 1), AW5T displays a subtle shoulder within the {200}<sub>c</sub> peak. This results in an apparent shift of the {200}<sub>c</sub> peak, suggesting that an increased amount of Ta can effectively mitigate the peak splitting. Previous research has shown that the separation of the {220}<sub>O</sub> and {008}<sub>O</sub> reflections indicates distortion in the oxygen octahedra [32]. Therefore, it can be deduced that Ta doping curbs this distortion [26–30], while W doping does not exert a similar effect. Moreover, considering Shannon's radii [33], Tantalum (Ta<sup>5+</sup>) and Niobium (Nb<sup>5+</sup>) ions share the same effective ionic radius (0.64 Å, CN = 6), while Tungsten (W<sup>6+</sup>) ion possesses a slightly smaller ionic radius of 0.60 Å (CN = 6). Owing to these small differences in ionic radius, any shifts in the peak indicating alterations in the lattice parameters are subtle.

Fig. 2 displays the BSE images of the ceramic samples' original surfaces. We have successfully produced dense ceramic specimens that exhibit tightly packed microstructures characterized by block-shaped granules. Remarkably, all samples lack any prominent secondary phases or significant defects. The mean grain size ranges between 2 and 5 μm, which is slightly smaller than the grain size of approximately 5 μm observed for pure AN [14]. It appears that doping with W slightly augments the grain size. However, Ta doping effectively inhibits grain growth, as depicted in Fig. 2. This can be ascribed to the increased Ta content requiring a higher sintering temperature, stemming from the refractory characteristics of Ta<sub>2</sub>O<sub>5</sub> [24]. Table 1 presents the EDS data for the ceramic samples, which generally confirms the accurate stoichiometry for each component, albeit with some margin of error.

Fig. 3 presents a set of plots including impedance spectroscopy (Z\* plots), combined Z''/M'' spectroscopic data, and Arrhenius plots for both AWx and AWxT ceramics. Within the context of impedance spectroscopy data, Z' signifies the imaginary component of Z\*, whereas M'' is calculated using formula  $M'' = 2\pi f \epsilon_0 Z'$  ( $f$  symbolizes the frequency measured in Hz,  $\epsilon_0$  equates to  $8.854 \times 10^{-14}$  F/cm, and Z' represents the real component of Z\*) [34]. All the ceramic samples demonstrate electrical homogeneity, signifying the presence of a single resistance-capacitance (RC) element, a trait suggestive of bulk-like behavior. This observation is corroborated by the emergence of a standard semicircle in the Z\* plot, coupled with a simultaneous Debye peak in both the -Z'' and M'' spectroscopic plots at an identical frequency [35,36]. The electrical conductivity ( $\sigma$ ) of the ceramics can be ascertained from their M'' Debye peak positions, using the formula  $2\pi f_{\max} RC = 1$ , where  $\sigma$  is the reciprocal of R, and C is defined as  $0.5\epsilon_0/M''$ . As shown in Fig. 3(a), (b) and (d), with Ta doping, the semicircles enlarge at the same temperature due to the reduction in electrical conductivity, correlating with lower frequency Debye peaks seen in Fig. 4(c) and (e). Earlier research on AN has indicated that the band gap is around 2.8 eV [37]. Consequently, the activation energy ( $E_a$ ) is half of the band gap value ( $E_g = 2.8$  eV), which equates to 1.4 eV. As shown in Fig. 3(f), The  $E_a$  for both AWx and AWxT ceramics, being less than 1 eV, is notably lower than the  $E_a$  of AN. This suggests that the electrical conduction behavior in AWx and AWxT ceramics might not align with the intrinsic electronic conduction. Aliovalent doping of W/Ta at the Nb-site coupled with vacancies at the Ag-site could potentially introduce some extrinsic conduction to enhance the electrical conductivity because the  $E_a$  for all the samples

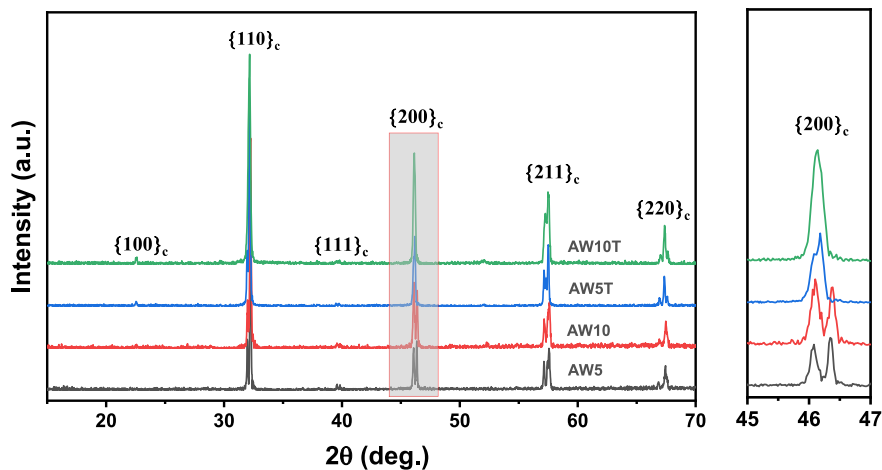


Fig. 1. XRD patterns and an enlarged view in the range of 45–47°.

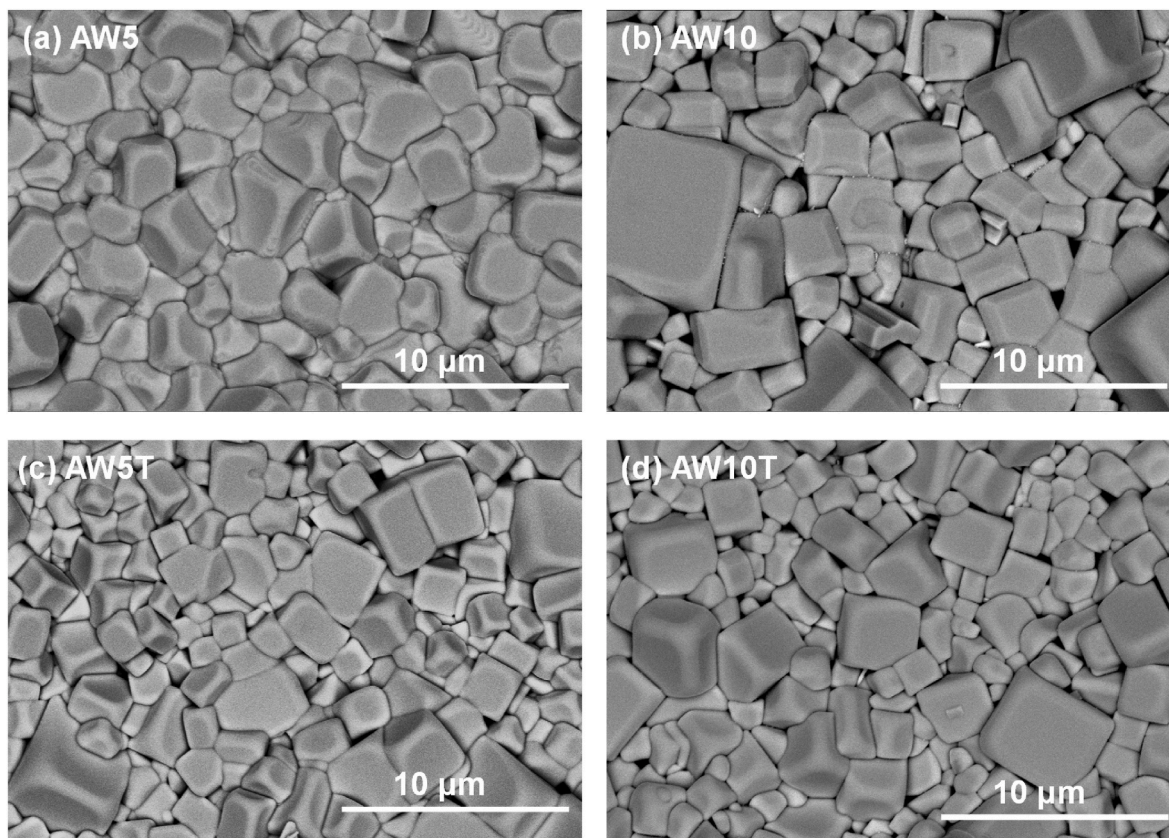


Fig. 2. BSE images of the original surface of the ceramic samples (a) AW5, (b) AW10, (c) AW5T, and (d) AW10T.

Table 1

Atomic percentages (at. %) derived from EDS spectra of various compositions.

Elements/Compositions	AW5	AW10	AW5T	AW10T
Ag	14.85	12.88	14.57	15.17
W	0.72	0.9	1.21	1.59
Nb	16.28	15.0	12.75	12.59
Ta	/	/	3.31	3.6
O	68.15	71.22	68.16	67.05

closely aligns with the  $E_a$  associated with ionic conduction or the migration of oxygen vacancies [38].

Fig. 4 portrays how the permittivity and dielectric loss of AWx and AWxT ceramics vary with temperature, measured across a frequency spectrum ranging from 10 kHz to 1 MHz. According to the literature, it is understood that for AN, the sequential phase transitions of M1-M2, M2-M3, M3-O, and O-T occur at approximate temperatures of 67 °C, 267 °C, 353 °C, and 387 °C, respectively [14]. When observing AW5, a derivative of AN, it similarly exhibits four distinct dielectric anomalies, aligning with the reported phase transitions M1-M2, M2-M3, M3-O, and

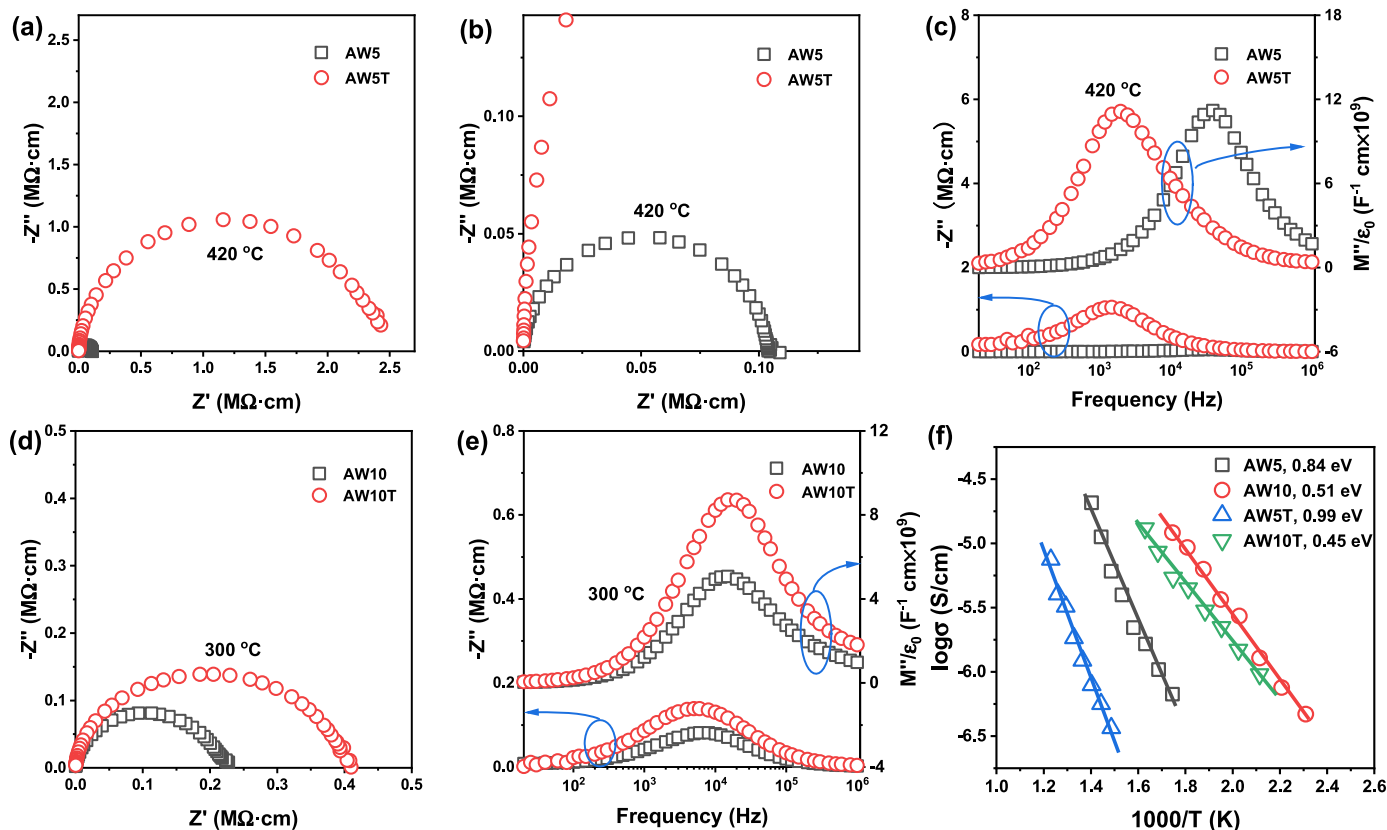


Fig. 3. (a)  $Z^*$  plots, (b) An enlarged view of (a), and (c)  $-Z''$  and  $M''$  spectroscopic plots of AW5 and AW5T ceramics at 420 °C; (d)  $Z^*$  plots and (e)  $-Z''$  and  $M''$  spectroscopic plots of AW10 and AW10T ceramics at 300 °C; (f) the Arrhenius plots of electrical conductivity extracted from  $M''$  spectroscopic plots.

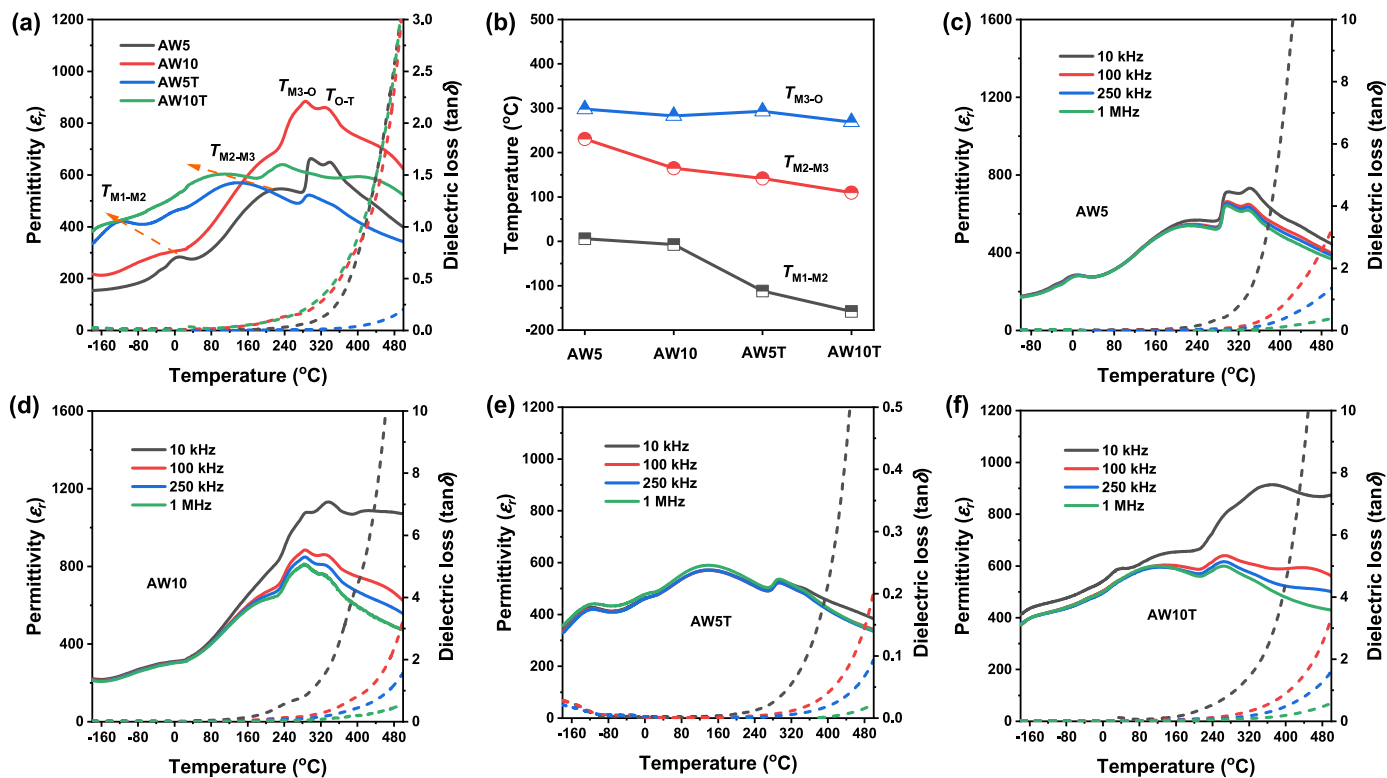


Fig. 4. (a) Temperature dependence of permittivity and dielectric loss of AWx and AWxT at 100 kHz; (b) phase transition temperatures for the AWx and AWxT ceramics; (c) AW5, (d) AW10, (e) AW5T, (f) AW10T.

O-T, as the temperature incrementally escalates from low to high, depicted in Fig. 4(a). With an increase in W content, there is a noticeable shift of all four phase transition temperatures to lower values, with  $T_{M1-M2}$  transitioning to temperatures below 0 °C. This implies a heightened stability of the antiferroelectric phase at room temperature. It is also observed that the M3-O and O-T phase transitions can be more distinctly separated due to the conspicuous nature of the O-T phase transition. However, this separation is compromised with the introduction of Ta doping, resulting in the O-T phase transitions becoming barely perceptible. In addition to these observations, it is noteworthy that the dielectric loss remains low up to a temperature of 500 °C. This characteristic demonstrates that all samples maintain a low level of electrical conductivity, a feature which is congruent with the impedance data illustrated in Fig. 3. The trend in the variation of the phase transition temperature following Ta doping is found to be consistent with our prior findings and other established research [16,25,30].

*In-situ* temperature (−193 to 227 °C) SXPd was performed to examine structural behavior of AW10. At −193 °C, the structure was best refined with single orthorhombic non-polar *Pbcm* structure, as shown in Fig. 5(a) below, which is in agreement with [25]. As increasing temperature to 150 °C, the best refined structure is obtained in a mixed phase of orthorhombic non-polar *Pbcm* and orthorhombic polar *Pmc2<sub>1</sub>*. These two structures are really similar with different polarizable axis. One refinement example (at 227 °C) is illustrated in Fig. 5(b), showing representative SXRD peaks consisted of mixed phases (Fig. 5c and d). Temperature dependence of high-resolution powder SXRD provides useful insights on the phase transition of AW10, which can be correlated

with temperature-dependent dielectric properties. There is no obvious structural transformation at phase transition temperature  $T_{M1-M2}$ , where a small anomaly is observed in Fig. 4(a), indicating this structural transformation may be related to local distortion. However, the phase transition temperature  $T_{M2-M3}$ , observed as a shoulder at ~155 °C in Fig. 4(a), is associated with the structural transformation from *Pbcm* to *Pmc2<sub>1</sub>*. Meanwhile, the frequency dispersion in permittivity curve is observed above 150 °C (Fig. 4(d)), which is also possible due to the emerging of *Pmc2<sub>1</sub>* phase.

All SXPd pattern from −193 to 227 °C was carried out full-pattern refinement and obtained crystallographic information was displayed in Fig. 6 and Table 2 below. All GOF is obtained to be 1.02–1.06. The orthorhombic non-polar *Pbcm* structure is found from −193 to 227 °C while orthorhombic polar *Pmc2<sub>1</sub>* phase is identified above 150 °C. Lattice parameter *a* and *b* of *Pbcm* phase change slightly ( $\pm 0.01$  Å) while lattice parameter *c*, increases significantly from 15.57 Å at −193 °C to 15.72 Å at 227 °C. The unit cell volume is also found to increase from approximately 480 Å<sup>3</sup> at −193 °C to 485 Å<sup>3</sup> at 227 °C. At 227 °C, the phase fraction of *Pbcm* and *Pmc2<sub>1</sub>* is approximately 55% and 45%, respectively. The persistence of the non-polar *Pbcm* phase, combined with the emergence of the new polar *Pmc2<sub>1</sub>* phase above 150 °C, aligns with the phase transition temperature  $T_{M2-M3}$  at approximately 160 °C in Fig. 4(a). This suggests that not all M2 phases undergo transformation into polar phases within the temperature range of 150–227 °C.

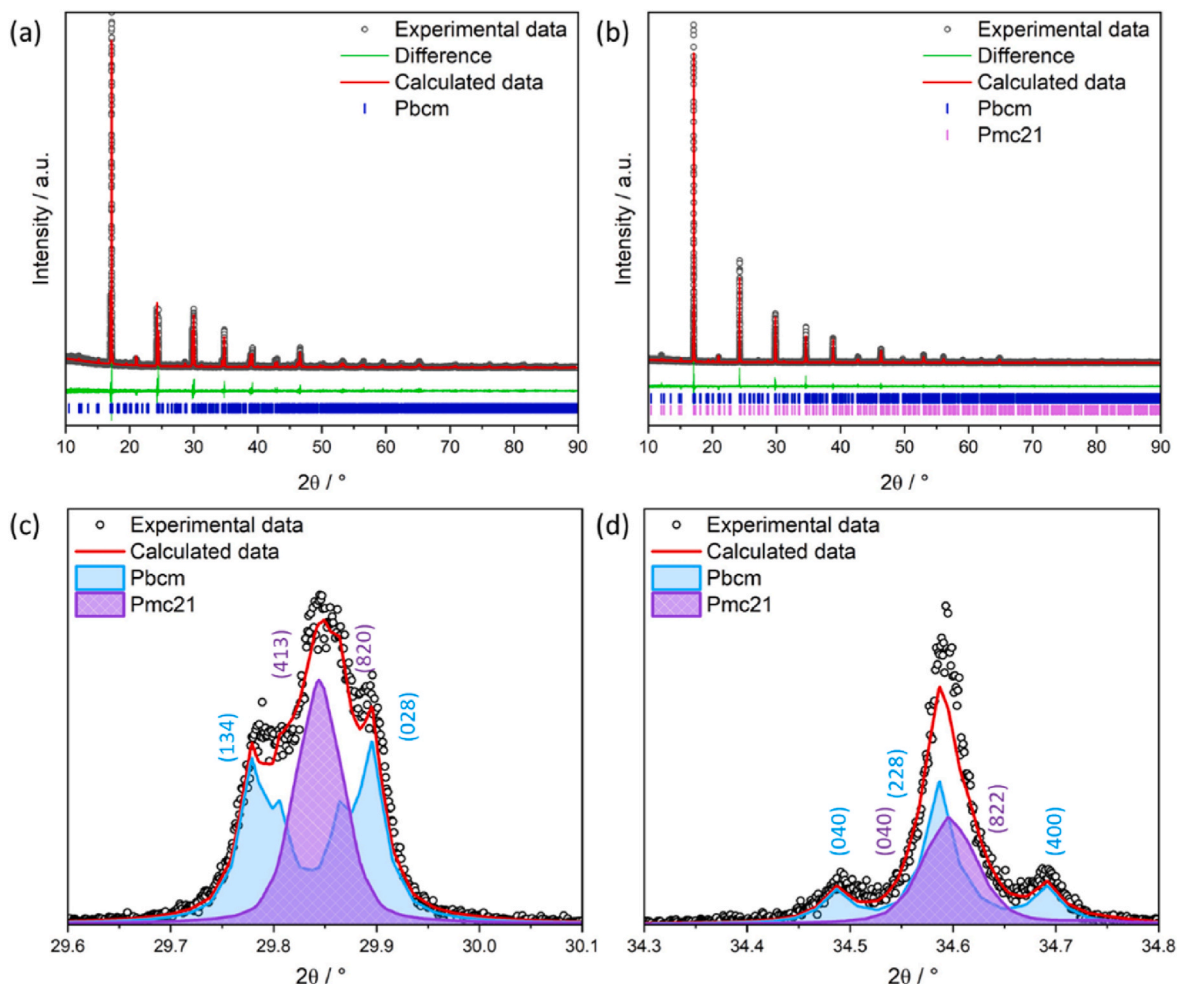


Fig. 5. Full-pattern refinement of AW10 at (a) −193 °C and (b) 227 °C. (c–d) Representative SXRD peak refinement using a mixed of *Pbcm* and *Pmc2<sub>1</sub>* phase of AW10.

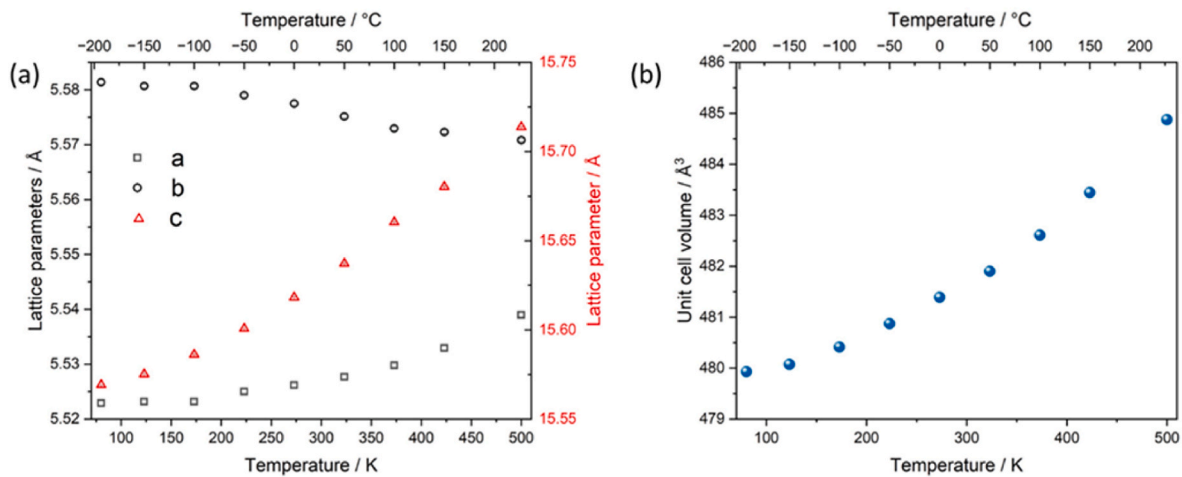


Fig. 6. Temperature-dependent (a) lattice parameters and (b) unit cell volume of *Pbcm* phase of AW10.

Table 2

Detailed crystallographic information of *Pmc2*<sub>1</sub> and *Pbcm* phases of AW10.

Temp/°C	<i>Pmc2</i> <sub>1</sub>					<i>Pbcm</i>					
	a/Å	b/Å	c/Å	V/Å <sup>3</sup>	Fraction	a/Å	b/Å	c/Å	V/Å <sup>3</sup>	Fraction	GOF
-193	N/A					5.52288	5.5814	15.56926	479.92826	100%	1.04
-150						5.52316	5.58068	15.57521	480.07432	100%	1.02
-100						5.52316	5.58067	15.58622	480.07391	100%	1.02
-50						5.52499	5.57898	15.60076	480.87525	100%	1.03
0						5.52617	5.5775	15.61828	481.38988	100%	1.04
50						5.52767	5.57514	15.63721	481.90046	100%	1.06
100						5.52978	5.57295	15.66042	482.60969	100%	1.06
150	15.67967	5.5679	5.53059	482.83633	42%	5.53296	5.57231	15.68027	483.44396	58%	1.03
227	15.71199	5.55359	5.55227	484.47957	45%	5.53896	5.57083	15.71382	484.87521	55%	1.03

#### 4. Conclusions

In this study, Tungsten (W) was successfully incorporated into the Nb-site, offset by vacancies at the Ag-site, which retains electrical homogeneity but introduces a degree of extrinsic conductivity. The antiferroelectric phase is stabilized via W doping as an increase in W content visibly shifts all four-phase transition (M1-M2, M2-M3, M3-O, and O-T) temperatures to lower values. There is also a clear observation that the M3-O and O-T phase transitions become more discernible after W doping. Introducing co-doping of W and 20 at% Tantalum (Ta) into the Nb-site can effectively suppress the electrical conductivity. However, it also hinders the separation of the M3-O and O-T phase transition peaks in temperature-dependent permittivity curves. Using *in-situ* high-resolution synchrotron powder x-ray diffraction (SPXD) at varying temperatures, it was demonstrated for the first time that in  $\text{Ag}_{0.9}\text{W}_{0.1}\text{Nb}_{0.9}\text{O}_3$ , the higher temperature M3 phase is a mix of orthorhombic non-polar *Pbcm* and orthorhombic polar *Pmc2*<sub>1</sub> within the temperature range of 150–227 °C. However, at temperatures below 150 °C, the non-polar *Pbcm* provides a more accurate representation of the crystallographic structure.

#### CRediT authorship contribution statement

**Zhilun Lu:** Conceptualization, Methodology, Investigation, Writing – original draft, Writing – review & editing, Supervision, Funding acquisition. **Yubo Zhu:** Investigation, Visualization. **Dongyang Sun:** Investigation, Visualization. **Bowen Wang:** Investigation, Visualization. **Dawei Wang:** Investigation, Writing – review & editing. **Sarah Day:** Investigation, Visualization. **Ge Wang:** Writing – review & editing, Supervision.

#### Declaration of competing interest

The authors declare that they have no known competing financial interests or personal relationships that could have appeared to influence the work reported in this paper.

#### Data availability

Data will be made available on request.

#### Acknowledgments

This work was supported by the Royal Society Research Grant (RGS \R1\221252). We thank Diamond Light Source for access to beamline11 (proposal number CY27232) that contributed to the results presented here.

#### References

- [1] K. Zou, Y. Dan, H. Xu, Q. Zhang, Y. Lu, H. Huang, Y. He, Recent advances in lead-free dielectric materials for energy storage, *Mater. Res. Bull.* 113 (2019) 190–201.
- [2] L. Yang, X. Kong, F. Li, H. Hao, Z. Cheng, H. Liu, J.-F. Li, S. Zhang, Perovskite lead-free dielectrics for energy storage applications, *Prog. Mater. Sci.* 102 (2019) 72–108.
- [3] X. Hao, A review on the dielectric materials for high energy-storage application, *J. Adv. Dielectr.* (2013), 1330001, 03(01).
- [4] G. Wang, Z. Lu, Y. Li, L. Li, H. Ji, A. Feteira, D. Zhou, D. Wang, S. Zhang, I. M. Reaney, Electroceramics for high-energy density capacitors: current status and future perspectives, *Chem. Rev.* 121 (10) (2021) 6124–6172.
- [5] Z. Sun, Z. Wang, Y. Tian, G. Wang, W. Wang, M. Yang, X. Wang, F. Zhang, Y. Pu, Progress, outlook, and challenges in lead-free energy-storage ferroelectrics, *Adv. Electron. Mater.* 6 (1) (2019), 1900698.
- [6] F. Zhuo, Q. Li, Y. Zhou, Y. Ji, Q. Yan, Y. Zhang, X. Xi, X. Chu, W. Cao, Large field-induced strain, giant strain memory effect, and high thermal stability energy

- storage in (Pb,La)(Zr,Sn,Ti)O<sub>3</sub> antiferroelectric single crystal, *Acta Mater.* 148 (2018) 28–37.
- [7] X. Wang, J. Shen, T. Yang, Y. Dong, Y. Liu, High energy-storage performance and dielectric properties of antiferroelectric (Pb<sub>0.97</sub>La<sub>0.02</sub>)(Zr<sub>0.5</sub>Sn<sub>0.5-x</sub>Ti<sub>x</sub>)O<sub>3</sub> ceramic, *J. Alloys Compd.* 655 (2016) 309–313.
- [8] H. Wang, Y. Liu, T. Yang, S. Zhang, Ultrahigh energy-storage density in antiferroelectric ceramics with field-induced multiphase transitions, *Adv. Funct. Mater.* 29 (7) (2019), 1807321.
- [9] A. Xie, R. Zuo, Z. Qiao, Z. Fu, T. Hu, L. Fei, NaNbO<sub>3</sub>-(Bi<sub>0.5</sub>Li<sub>0.5</sub>)TiO<sub>3</sub> lead-free relaxor ferroelectric capacitors with superior energy-storage performances via multiple synergistic design, *Adv. Energy Mater.* 11 (28) (2021), 2101378.
- [10] A. Xie, J. Fu, R. Zuo, X. Jiang, T. Li, Z. Fu, Y. Yin, X. Li, S. Zhang, Supercritical relaxor nanograined ferroelectrics for ultrahigh-energy-storage capacitors, *Adv. Mater.* 34 (34) (2022), 2204356.
- [11] M.H. Zhang, H. Ding, S. Egert, C. Zhao, L. Villa, L. Fulanovic, P.B. Groszewicz, G. Buntkowsky, H.J. Kleebe, K. Albe, A. Klein, J. Koruza, Tailoring high-energy storage NaNbO<sub>3</sub>-based materials from antiferroelectric to relaxor states, *Nat. Commun.* 14 (1) (2023), 1525.
- [12] A. Xie, H. Qi, R. Zuo, A. Tian, J. Chen, S. Zhang, An environmentally-benign NaNbO<sub>3</sub> based perovskite antiferroelectric alternative to traditional lead-based counterparts, *J. Mater. Chem. C* 7 (48) (2019) 15153–15161.
- [13] Z. Chen, S. Mao, L. Ma, G. Luo, Q. Feng, Z. Cen, F. Toyohisa, X. Peng, L. Liu, H. Zhou, C. Hu, N. Luo, Phase engineering in NaNbO<sub>3</sub> antiferroelectrics for high energy storage density, *J. Materiomics* 8 (4) (2022) 753–762.
- [14] Y. Tian, L. Jin, H. Zhang, Z. Xu, X. Wei, E.D. Politova, S. Yu Stefanovich, N. V. Tarakina, I. Abrahams, H. Yan, High energy density in silver niobate ceramics, *J. Mater. Chem. A* 4 (44) (2016) 17279–17287.
- [15] D. Yang, J. Gao, L. Shu, Y.-X. Liu, J. Yu, Y. Zhang, X. Wang, B.-P. Zhang, J.-F. Li, Lead-free antiferroelectric niobates AgNbO<sub>3</sub> and NaNbO<sub>3</sub> for energy storage applications, *J. Mater. Chem. A* 8 (2020) 23724–23737.
- [16] Z. Lu, W. Bao, G. Wang, S.-K. Sun, L. Li, J. Li, H. Yang, H. Ji, A. Feteira, D. Li, F. Xu, A.K. Kleppe, D. Wang, S.-Y. Liu, I.M. Reaney, Mechanism of enhanced energy storage density in AgNbO<sub>3</sub>-based lead-free antiferroelectrics, *Nano Energy* 79 (2021), 105423.
- [17] D. Fu, M. Endo, H. Taniguchi, T. Taniyama, M. Itoh, AgNbO<sub>3</sub>: a lead-free material with large polarization and electromechanical response, *Appl. Phys. Lett.* 90 (25) (2007), 252907.
- [18] J. Gao, Y. Zhang, L. Zhao, K.-Y. Lee, Q. Liu, A. Studer, M. Hinterstein, S. Zhang, J.-F. Li, Enhanced antiferroelectric phase stability in La-doped AgNbO<sub>3</sub>: perspectives from the microstructure to energy storage properties, *J. Mater. Chem. A* 7 (5) (2019) 2225–2232.
- [19] N. Luo, K. Han, F. Zhuo, L. Liu, X. Chen, B. Peng, X. Wang, Q. Feng, Y. Wei, Design for high energy storage density and temperature-insensitive lead-free antiferroelectric ceramics, *J. Mater. Chem. C* 7 (17) (2019) 4999–5008.
- [20] S. Li, H. Nie, G. Wang, C. Xu, N. Liu, M. Zhou, F. Cao, X. Dong, Significantly enhanced energy storage performance of rare-earth-modified silver niobate lead-free antiferroelectric ceramics via local chemical pressure tailoring, *J. Mater. Chem. C* 7 (6) (2019) 1551–1560.
- [21] K. Han, N. Luo, S. Mao, F. Zhuo, X. Chen, L. Liu, C. Hu, H. Zhou, X. Wang, Y. Wei, Realizing high low-electric-field energy storage performance in AgNbO<sub>3</sub> ceramics by introducing relaxor behaviour, *J. Materiomics* 5 (4) (2019) 597–605.
- [22] J. Gao, Q. Liu, J. Dong, X. Wang, S. Zhang, J.F. Li, Local structure heterogeneity in Sm-doped AgNbO<sub>3</sub> for improved energy-storage performance, *ACS Appl. Mater. Interfaces* 12 (5) (2020) 6097–6104.
- [23] Y. Tian, L. Jin, H. Zhang, Z. Xu, X. Wei, G. Viola, I. Abrahams, H. Yan, Phase transitions in bismuth-modified silver niobate ceramics for high power energy storage, *J. Mater. Chem. A* 5 (33) (2017) 17525–17531.
- [24] N. Luo, K. Han, M.J. Cabral, X. Liao, S. Zhang, C. Liao, G. Zhang, X. Chen, Q. Feng, J.F. Li, Y. Wei, Constructing phase boundary in AgNbO<sub>3</sub> antiferroelectrics: pathway simultaneously achieving high energy density and efficiency, *Nat. Commun.* 11 (1) (2020), 4824.
- [25] Y. Tian, L. Jin, Q. Hu, K. Yu, Y. Zhuang, G. Viola, I. Abrahams, Z. Xu, X. Wei, H. Yan, Phase transitions in tantalum-modified silver niobate ceramics for high power energy storage, *J. Mater. Chem. A* 7 (2) (2019) 834–842.
- [26] K. Han, N. Luo, S. Mao, F. Zhuo, L. Liu, B. Peng, X. Chen, C. Hu, H. Zhou, Y. Wei, Ultrahigh energy-storage density in A-/B-site co-doped AgNbO<sub>3</sub> lead-free antiferroelectric ceramics: insight into the origin of antiferroelectricity, *J. Mater. Chem. A* 7 (46) (2019) 26293–26301.
- [27] L. Zhao, Q. Liu, S. Zhang, J.-F. Li, Lead-free AgNbO<sub>3</sub> anti-ferroelectric ceramics with an enhanced energy storage performance using MnO<sub>2</sub> modification, *J. Mater. Chem. C* 4 (36) (2016) 8380–8384.
- [28] C. Xu, Z. Fu, Z. Liu, L. Wang, S. Yan, X. Chen, F. Cao, X. Dong, G. Wang, La/Mn codoped AgNbO<sub>3</sub> lead-free antiferroelectric ceramics with large energy density and power density, *ACS Sustain. Chem. Eng.* 6 (12) (2018) 16151–16159.
- [29] N. Luo, K. Han, F. Zhuo, C. Xu, G. Zhang, L. Liu, X. Chen, C. Hu, H. Zhou, Y. Wei, Alivalent A-site engineered AgNbO<sub>3</sub> lead-free antiferroelectric ceramics toward superior energy storage density, *J. Mater. Chem. A* 7 (23) (2019) 14118–14128.
- [30] S. Gao, Y. Huang, Y. Jiang, M. Shen, H. Huang, S. Jiang, Y. He, Q. Zhang, Ultrahigh energy density and excellent discharge properties in Ce<sup>4+</sup> and Ta<sup>5+</sup> co-modified AgNbO<sub>3</sub> relaxor antiferroelectric ceramics via multiple design strategies, *Acta Mater* 246 (2023), 118730.
- [31] Z. Lu, D. Sun, G. Wang, J. Zhao, B. Zhang, D. Wang, I. Shyha, Energy storage properties in Nd-doped AgNbTaO<sub>3</sub> lead-free antiferroelectric ceramics with Nb-site vacancies, *J. Adv. Dielectr.* 13 (2023), 2242006, 01.
- [32] I. Levin, J.C. Woicik, A. Llobet, M.G. Tucker, V. Krayzman, J. Pokorny, I. M. Reaney, Displacive ordering transitions in perovskite-like AgNb<sub>1/2</sub>Ta<sub>1/2</sub>O<sub>3</sub>, *Chem. Mater.* 22 (17) (2010) 4987–4995.
- [33] R.D. Shannon, Revised effective ionic radii and systematic studies of interatomic distances in halides and chalcogenides, *Acta Crystallogr.* A32 (1976) 751–767.
- [34] J.T.S. Irvine, D.C. Sinclair, A.R. West, Electroceramics characterization by impedance spectroscopy, *Adv. Mater.* 2 (3) (1990) 132–138.
- [35] Z. Lu, G. Wang, L. Li, Y. Huang, A. Feteira, W. Bao, A.K. Kleppe, F. Xu, D. Wang, I. M. Reaney, In situ poling X-ray diffraction studies of lead-free BiFeO<sub>3</sub>-SrTiO<sub>3</sub> ceramics, *Mater. Today Phys.* 19 (2021), 100426.
- [36] Z. Lu, G. Wang, W. Bao, J. Li, L. Li, A. Mostaed, H. Yang, H. Ji, D. Li, A. Feteira, F. Xu, D.C. Sinclair, D. Wang, S.-Y. Liu, I.M. Reaney, Superior energy density through tailored dopant strategies in multilayer ceramic capacitors, *Energy Environ. Sci.* 13 (9) (2020) 2938–2948.
- [37] H.K. Hideki Kato, Akihiko Kudo, Role of Ag<sup>+</sup> in the band structures and photocatalytic properties of AgMO<sub>3</sub> (M Ta and Nb) with the perovskite structure, *J. Phys. Chem. B* 106 (2002) 12441–12447.
- [38] R. Muduli, R. Pattanayak, S. Raut, P. Sahu, S. V. S. Rath, P. Kumar, S. Panigrahi, R. K. Panda, Dielectric, ferroelectric and impedance spectroscopic studies in TiO<sub>2</sub>-doped AgNbO<sub>3</sub> ceramic, *J. Alloys Compd.* 664 (2016) 715–725.